Vanadium-doped $LiNi_{1/3}Co_{1/3}Mn_{1/3}O_2$ with decreased lithium/nickel disorder as high-rate and long-life lithium ion battery cathode

Zhengyao Hu, Luoluo Wang, Yanzhu Luo, Qiulong Wei, Mengyu Yan, Liang Zhou and Liqiang Mai[*]

State Key Laboratory of Advanced Technology for Materials Synthesis and Processing,
Wuhan University of Technology, Wuhan 430070, P. R. China

[*]Author for correspondence: Liqiang Mai, email: mlq518@whut.edu.cn

Layered lithium transition metal oxides have attracted significant interest as the cathode material for lithium ions batteries owing to their high capacity. However, their poor cycle life and rate capability limit their widespread use in large scale. Herein, we report a vanadium-doped $LiNi_{1/3}Co_{1/3}Mn_{1/3}O_2$ cathode material. The introduction of vanadium leads to increase in the concentration of trivalent manganese ions. The increased Mn^{3+} facilitates the diffusion of lithium ions and electrons, reduces the lithium/nickel disorder, and stabilizes the crystal structure during lithiation/de-lithiation processes. The vanadium-doped $LiNi_{1/3}Co_{1/3}Mn_{1/3}O_2$ shows prominent high-rate and long-life capability. An initial specific capacity of 138 mAh g^{-1} is obtained at a high rate of 20 C. A specific capacity of 161 mAh g^{-1} is achieved at 1 C, maintaining 114 mAh g^{-1} after 1000 cycles. The excellent electrochemical performance makes the vanadium-doped $LiNi_{1/3}Co_{1/3}Mn_{1/3}O_2$ a very promising cathode material for lithium ion batteries.

1. INTRODUCTION

In recent years, the rapid development of electric vehicles puts forward high demand for rechargeable lithium ion batteries (LIBs). Many researchers are concentrating on the cathode materials with high capacity and high-rate capability. The application of traditional layered $LiCoO_2$ suffers from high costs, safety hazards, and environmental toxicity, despite widely used in commercial LIBs [1]. Considering these drawbacks of $LiCoO_2$, $LiNi_xCo_yMn_{[1-x-y]}O_2$ have been explored as one of the most promising cathode candidates for high-performance LIBs. Their low costs, high capacity and energy density, reliable safety, and low toxicity have attracted extensive attentions worldwide [2-3]. Among the series of $LiNi_xCo_yMn_{[1-x-y]}O_2$, layered $LiNi_{1/3}Co_{1/3}Mn_{1/3}O_2$ (denoted as LNCM) is the most representative. Its crystal structure belongs to the α-$NaFeO_2$ type with a rhombohedral R$\bar{3}$m symmetry. Generally, electrochemical active nickel and cobalt produce high capacity by changing their valence states involving Ni^{2+}/Ni^{4+} and Co^{3+}/Co^{4+} redox couples [4], while inactive manganese ions stabilize the crystal structure and lower the costs.

Nevertheless, the performance of pristine $LiNi_{1/3}Co_{1/3}Mn_{1/3}O_2$ is rather limited, because of the Li^+/Ni^{2+} disorder in lattice, which leads to irreversible capacity loss [5]. The increased disorder also has negative impact on the rate capability and cycling life. To solve these problems, various strategies have been proposed, such as coating with carbon and metal oxides [6,7], fabricating porous micro/nano-structures [8], and doping [9-16]. Among these methods, doping is one of the most effective strategies to reduce the Li^+/Ni^{2+} disorder and improve the performance.

Various elements (such as Mg [9], Al [10], Zr [11], Fe [12], Cr [13], V [14], F [15,16], etc.) have been introduced into lithium transition metal oxides. Vanadium is an attractive active dopant because of its various valence states and outstanding electrochemical activity [17,18]. Sun et al. reported V-doped $LiFePO_4$ with improved high-rate capability, which was attributed to the increased ions diffusion coefficient [19]. Dai et al. found that proper amount of V^{3+} doping in $LiMnPO_4$ lead to a reduced charge transfer resistance [20]. Zhang et al. studied the electrochemical performance and mechanism of V-doping in Li_2FeSiO_4, which exhibited increased electronic conductivity, decreased charge transfer impedance, and improved Li-ion diffusion coefficient [21]. Hence, we suppose that vanadium-doping is a promising method to reduce the Li^+/Ni^{2+} disorder, and increase the charge transfer ability of LNCM.

In this work, we synthesized a vanadium-doped LNCM by a conventional co-precipitation method followed by annealing. The structural characterization and electrochemical measurements are carried out to study the properties of the vanadium-doped $LiNi_{1/3}Co_{1/3}Mn_{1/3}O_2$ (denoted as V-LNCM). The results indicate that V-LNCM manifests enhanced high-rate capability (138 mAh g^{-1} at 20 C) and superior long-cycling stability (114 mAh g^{-1} at 1 C after 1000 cycles).

2. MATERIALS AND METHODS

The LNCM and V-LNCM were prepared via a traditional co-precipitation method followed by annealing. $NiSO_4 \cdot 6H_2O$, $CoSO_4 \cdot 7H_2O$,
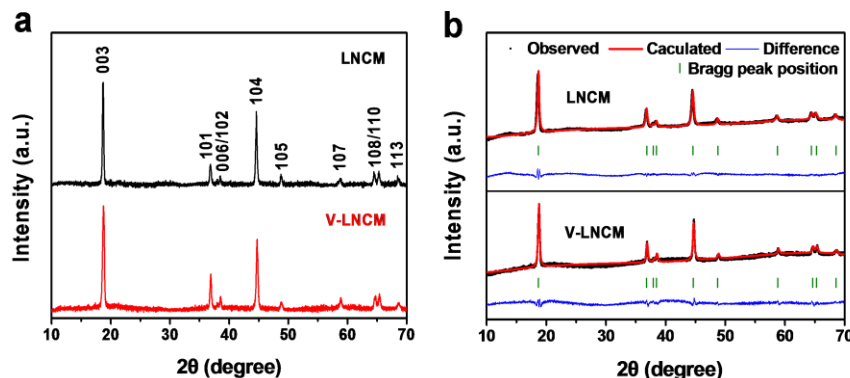
Figure 1. (a) XRD patterns, (b) Rietveld refinement patterns of LNCM and V-LNCM.

Table 1. Lattice parameters and chemical compositions of LNCM and V-LNCM.

Samples	a (Å)	c (Å)	c/a	Cell volume (Å^3)
LNCM	2.8607(3)	14.2271(4)	4.9733	100.8335
V-LNCM	2.8554(2)	14.1769(6)	4.9649	100.1049
Rietveld refinement				
LNCM	$(Li_{0.9663}Ni_{0.03772})(Ni_{0.2905}Li_{0.03772})Co_{0.3384}Mn_{0.3373}O_2$			
V-LNCM	$(Li_{0.9815}Ni_{0.01849})(Ni_{0.3146}Li_{0.01849})Co_{0.3336}Mn_{0.3248}V_{0.01}O_2$			
ICP investigation				
LNCM	$Li_{1.008}Ni_{0.3328}Co_{0.3327}Mn_{0.3345}O_2$			
V-LNCM	$Li_{1.002}Ni_{0.3340}Co_{0.3380}Mn_{0.3230}V_{0.0101}O_2$			

$MnSO_4 \cdot H_2O$ (molar ratio of Ni: Co: Mn=1: 1: 0.97) and stoichiometric Na_2CO_3 were dissolved in deionized water to get a 2 mol L^{-1} mixed sulfate solution and alkalinity solution, respectively. A desired amount of concentrated NH_4OH solution was diluted in 40 ml H_2O, then mixed sulfate solution and Na_2CO_3 alkaline solution were dropped into the solution containing diluted NH_4OH with the pH controlled at 8.0 under continuous stiring for 48 h at 65 °C. The as-prepared precipitation was centrifuged and then dried in air oven at 80 °C overnight to get a precursor powder. The obtained precursor was preheated at 500 °C for 5 h to get a dark powder, which was ground with stoichiometric $LiOH \cdot H_2O$ and then calcined at 800 °C for 16 h to synthesize the LNCM. For V-LNCM, stoichiometric $LiOH \cdot H_2O$ and V_2O_5 (molar ratio of Li: M: V=1: 0.99: 0.01, M represents transition metals) were ground with the dark powder followed by annealing at 800 °C for 16 h.

The crystal structures of LNCM and V-LNCM were studied by X-ray powder diffraction (XRD, Bruker D8 Advance) with non-monochromated Cu Kα X-Ray source. The morphologies of LNCM and V-LNCM were obtained on field emission scanning electron microscope (FESEM, JEOL JSM-7100F, 10 kV) and high-resolution transmission electron microscope (HRTEM, JEOL JEM-2100F, 200 kV). X-ray photoelectronic spectrometer (XPS, VGESCA-LABMK II) and an inductively coupled plasma mass spectroscopy (ICP-MS, Perkin-Elmer Optima 2100DV) were used to determine the composition of the products.

The positive electrode was prepared by casting a slurry containing active material (70 wt.%), Super P carbon (20 wt.%), and poly(vinylidene fluoride) (PVDF, 10 wt.%) dissolved in 1-methyl-2-pyrrolidinone (NMP) onto aluminum foil. Then, the electrode was dried in an oven at 80 °C overnight. The electrochemical performances of the LNCM and V-LNCM were evaluated using CR2025 coin cells assembled with a positive electrode, a lithium metal anode, a porous polypropylene film (Celgard 2400) as the separator, and 1 M lithium hexafluoro-phosphate ($LiPF_6$) dissolved in ethylene carbonate (EC) and dimethyl carbonate (DMC) (1:1 v/v) as the electrolyte in an argon-filled (O_2 and H_2O content < 0.1 ppm) glove box. Before charge/discharge processes, the cells were aged for 24 h to ensure full absorption of the electrolyte

into the electrodes. Galvanostatic charge/discharge tests were performed in the voltage range of 3.0 to 4.3 V at different current densities on a multichannel battery testing system (LAND CT2001A). The cells were charged under constant current and constant voltage (CCCV) mode, which was then discharged under constant current (CC) mode. The constant current charging is followed by a potentiostatic holding at 4.3 V until the current drops to 5% of charging current. The cells were then discharged to 3.0 V. Cyclic voltammetry (CV) test of cells was carried out with an electrochemical workstation (CHI 760D). The electrochemical impedance spectroscopy (EIS) was tested using another electrochemical workstation (Autolab PGSTAT 302N) at the cell voltage of 4.3 V in the frequency range 100 kHz to 0.01 Hz. All the tests were performed at room temperature.

3. RESULTS AND DISCUSSION

Figure 1a shows the XRD patterns of LNCM and V-LNCM. All peaks can be indexed to a hexagonal α-NaFeO$_2$ structure (space group, R$\bar{3}$m), while no impurity peak is detected. In the XRD patterns, the (006)/(102) and (108)/(110) peaks split up clearly, evidencing a typical layered structure [22]. Generally, the integrated intensity ratio of the (003) to (104) peaks is regarded as an evaluation of the cations-mixing in the layered structure [23]. When the value of I_{003}/I_{104} is below 1.2, there would be a mass of cations mixing in the crystal structure [24]. For as-prepared LNCM and V-LNCM, the values of I_{003}/I_{104} are 1.34 and 1.47, respectively, demonstrating that both samples have a low Li^+/Ni^{2+} disorder. From the magnified XRD patterns (Figure S1a), it is noticed that all the peaks of V-LNCM shift slightly toward high angle. When combined with oxygen to form O_6 octahedra, the vanadium (IV or V) shows an approximate effective radius to those of Co (III), Ni (III), and Mn (III or IV) (Table S1). Thus, it can be conjectured that the vanadium would enter the transitional metal layer due to their approximate radius. The precise chemical compositions of LNCM and V-LNCM are determined by the ICP investigation (Table 1), which are highly consistent with the feeding ratio.

Table 2. Rietveld refinement parameters of LNCM and V-LNCM.

Atom	site	x	y	z	Occ	
					LNCM	V-LNCM
Li1	$3a$	0	0	0	0.9663	0.9815
Ni1	$3b$	0	0	0.5	0.2905	0.3146
Co1	$3b$	0	0	0.5	0.3384	0.3336
Mn1	$3b$	0	0	0.5	0.3373	0.3248
V1	$3b$	0	0	0.5	——	0.01
O1	$6c$	0	0	0.23978/0.23889	1	1
Li2	$3b$	0	0	0.5	0.03772	0.01849
Ni2	$3a$	0	0	0	0.03772	0.01849
R_{wp}					1.88	2.91
R_p					1.43	2.29
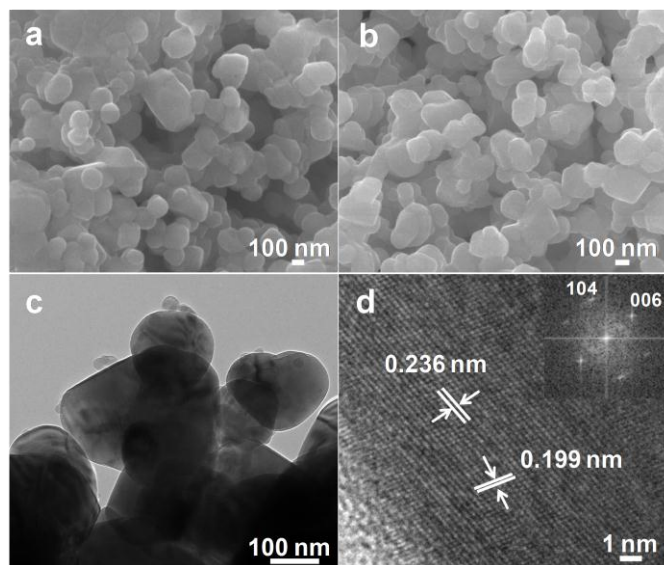
Figure 2. SEM images of LNCM (a) and V-LNCM (b), TEM image (c) and HRTEM image (d) of V-LNCM.

In order to understand the influence of V-doping on the structure of $LiNi_{1/3}Co_{1/3}Mn_{1/3}O_2$, Rietveld refinements are carried out for LNCM and V-LNCM (Figure 1b). The lattice parameters of LNCM and V-LNCM are shown in Table 1. The lattice parameters (a and c) decrease after the introduction of vanadium, which indicates that the dopant is incorporated into the crystal lattice [25]. And this result is consistent with the right-shift of XRD peaks in Figure S1a. At the same time, the high c/a values indicate a well-defined hexagonal α-$NaFeO_2$ structure. The detailed Rietveld refinement parameters are displayed in Table 2. The R_{wp} (instrument pattern factor) values of LNCM and V-LNCM are 1.88 and 2.91, which demonstrate the reliable Rietveld refinement results. By doping vanadium into LNCM, the disorder degree of Li^+/Ni^{2+} reduces from 3.77% to 1.85%, which is consistent with previous reports [14]. Rietveld refinement results indicate that vanadium occupies about 1% of $3b$ sites in transitional metal layer.

The morphologies of the precursor of LNCM and V-LNCM are shown in Figure S1b and S1c. It can be observed that the $Ni_{1/3}Co_{1/3}Mn_{1/3}CO_3$ precursor particles are agglomerated loosely. After sintering at 800 °C for 16 h, the size of the primary particles ranges from 100 nm to 300 nm with a relatively homogeneous distribution, which can be perceived distinctly from Figure 2a and 2b. The similarity between LNCM and V-LNCM in morphology illustrates that vanadium-doping has no impact on the morphology of $LiNi_{1/3}Co_{1/3}Mn_{1/3}O_2$. The microstructure of V-LNCM is further investigated by TEM images (Figure 2c and 2d). In HRTEM image, lattice fringes with interplanar spacings of 0.236 nm and

0.199 nm can be clearly observed, which can be indexed as the (006) and (104) planes of layered $LiNi_{1/3}Co_{1/3}Mn_{1/3}O_2$.

To further investigate the influence of vanadium-doping on layered $LiNi_{1/3}Co_{1/3}Mn_{1/3}O_2$, XPS measurements are adopted to comprehend the oxidation state of transition metals, and the corresponding spectra are presented in Figure 3 and Figure S2. The survey spectra confirm the presence of Li, Ni, Co, Mn, V, C and O, in which the C comes from the contaminants and no other impurity is detected. After calibrating the binding energies obtained in the XPS analysis by referencing the C1s line to 284.63 eV, the binding energies of dominant peaks are 54.22, 854.7, 779.9, 642.35, 516.7, and 529.56 eV, which are attributed to Li^+, Ni^{2+}, Co^{3+}, Mn^{4+}, V^{5+} and O^{2-} in V-LNCM, respectively [6-26].

The peaks of Ni2p, Co2p, Mn2p and V2p spectra in Figure 3 are acquired by using a Lorentzian-Gaussian fitting method. The fitting results in Figure 3a indicate that there are two kinds of valence states for Ni in 2p3/2 and 2p1/2 orbits. The peaks locate at 854.70 and 861.08 eV are the characteristic Ni2p3/2 peaks of Ni^{2+}, while the peaks at 872.01 and 879.06 eV come from the Ni2p1/2 peaks of Ni^{2+}. Additionally, two weak fitting peaks at 856.97 and 873.70 eV prove the existence of Ni^{3+} [27]. The fitting area of peaks can reflect the content of Ni in different valence states to a certain extent, which means the Ni^{2+} is the primary existing form for Ni in the lattice. Similarly, the primary valence state of Co in the lattice is trivalent, which can be seen from the Co2p spectra in Figure 3b. The two major peaks of Co2p3/2 and Co2p1/2 with a spin-orbit splitting of 15.0 eV locate at 779.9 and 794.9 eV [28], and a weak shake-up satellite peak at 789.73 eV, about 9.5 eV above the Co mainline, is observed, which is the fingerprint of Co^{3+} [29]. The appearance of two weak peaks at 781.73 and 798.51 eV demonstrated the coexistence of Co^{2+}. The Mn2p spectra in Figure 3c also show two main spin-orbit lines of 2p3/2 at 642.35 eV and 2p1/2 at 653.7 eV with separation of 11.35 eV, indicating the dominant Mn^{4+}. However, a couple of less prominent peaks at 644.16 and 655.71 eV are characteristic of Mn^{3+} [30]. Figure 3d reveals the V2p spectrum, in which the two prominent peaks are sitting at 516.7 and 519.38 eV, corresponding to the V2p3/2 and V2p1/2 peaks, respectively. The XPS results indicate that the oxidation valence state of vanadium element in V-LNCM is pentavalent [31].

For LNCM and V-LNCM, the main valence states of Ni, Co, Mn are Ni^{2+}, Co^{3+}, Mn^{4+}. V-LNCM has similar content of Ni^{3+} and Co^{2+} with LNCM, but higher content of Mn^{3+} (17.05%) than LNCM (13.59%). As reported by Shaju et al. [26], the origin of Mn^{3+} and Ni^{3+} in the lattice are due to the electron transfer between Mn^{4+} and Ni^{2+} pairs, leading to small amount of valency-degeneracy by the dynamic equilibrium: $Mn^{4+} + Ni^{2+} \rightarrow Mn^{3+} + Ni^{3+}$. In the present case, the content of Mn^{3+} is higher than the calculated value by the dynamic equilibrium. Hence, we attribute the mainly increase of Mn^{3+} in V-LNCM to vanadium doping (extra 1% positive charge due to V^{5+}).

The electrochemical properties of V-LNCM and LNCM are investigated at 0.5-20 C in the voltage range of 3.0–4.3 V at room temperature in coin-type cells. When cycling at 1 C (1 C = 160 mA g^{-1})
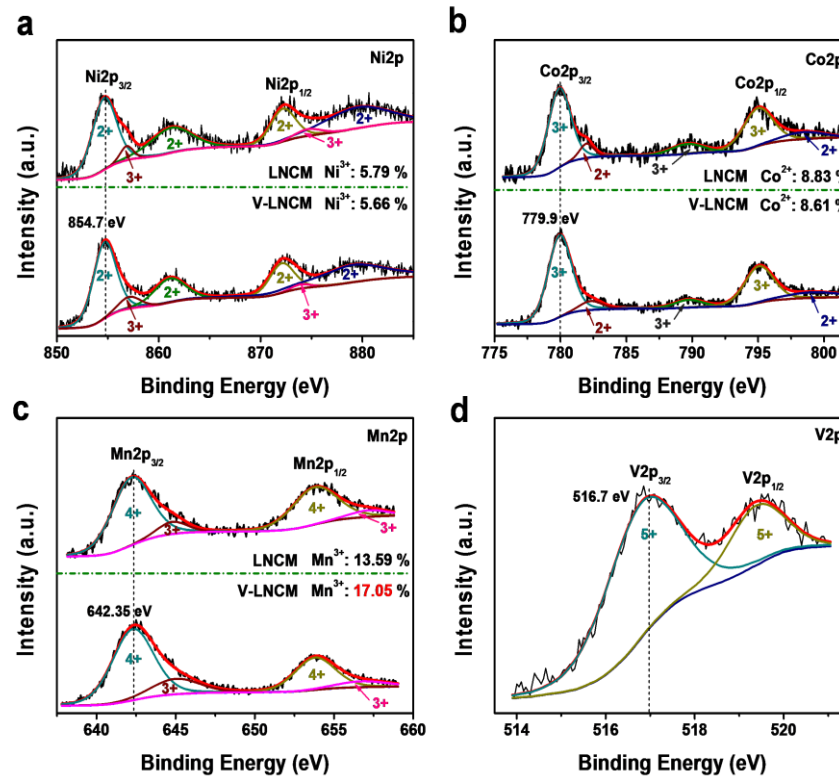
Figure 3. XPS spectra of Ni2p (a), Co2p (b), Mn2p (c) and V2p (d) for LNCM and V-LNCM.
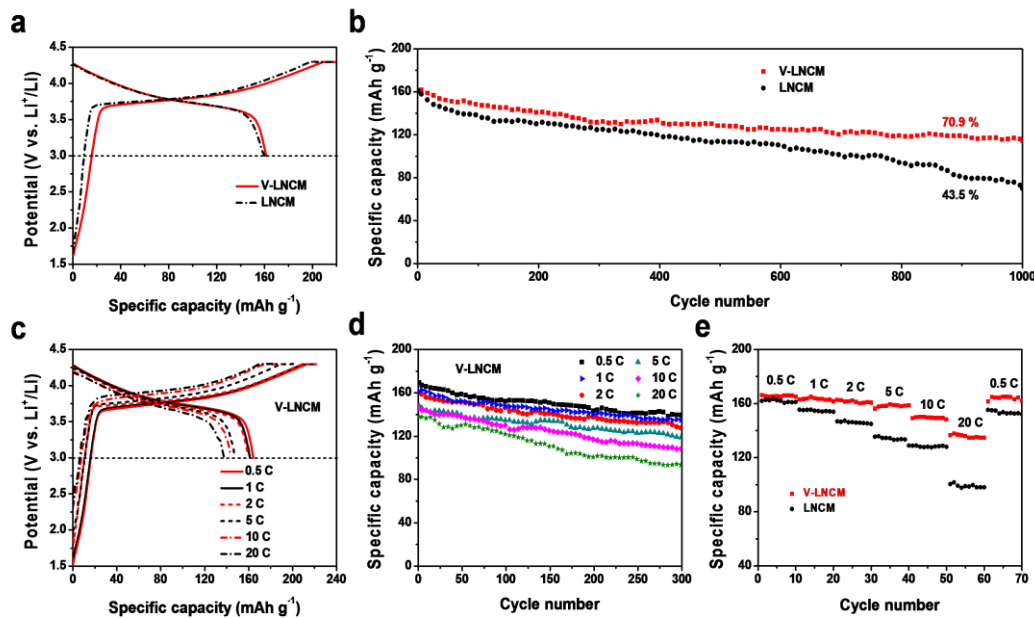
Figure 4. Electrochemical characteristics: (a) Initial charge-discharge profiles of LNCM and V-LNCM, (b) Cycling performances of the LNCM and V-LNCM at 1 C for 1000 cycles in 3.0–4.3 V, (c) Initial charge-discharge profiles of the V-LNCM at different rates, (d) Cycling performances of V-LNCM at different current densities from 0.5 C to 20 C, (e) Rate performances of LNCM and V-LNCM.

(Figure 4a), the LNCM delivers an initial charge capacity of 204 mAh g^{-1} and a subsequent discharge capacity of 159 mAh g^{-1}. The initial charge and discharge capacities of V-LNCM are 218 and 161 mAh g^{-1}, respectively. The shapes of the curves are in good agreement with previous literatures [32]. During the first charge process, partial Ni^{2+} would occupy the lithium site, hindering the intercalation of Li^{+}. This results in the initial irreversible capacity loss [5]. Long-life cycling performance at 1 C is shown in Figure 4b and the corresponding charge-discharge profiles at different cycles are shown in Figure S3. The V-LNCM delivers a remarkable capacity of 114 mAh g^{-1} after 1000 cycles, corresponding to a capacity retention of 70.9%. This value is much higher than that of LNCM (43.5%). Figure 4c displays the charge-discharge

4
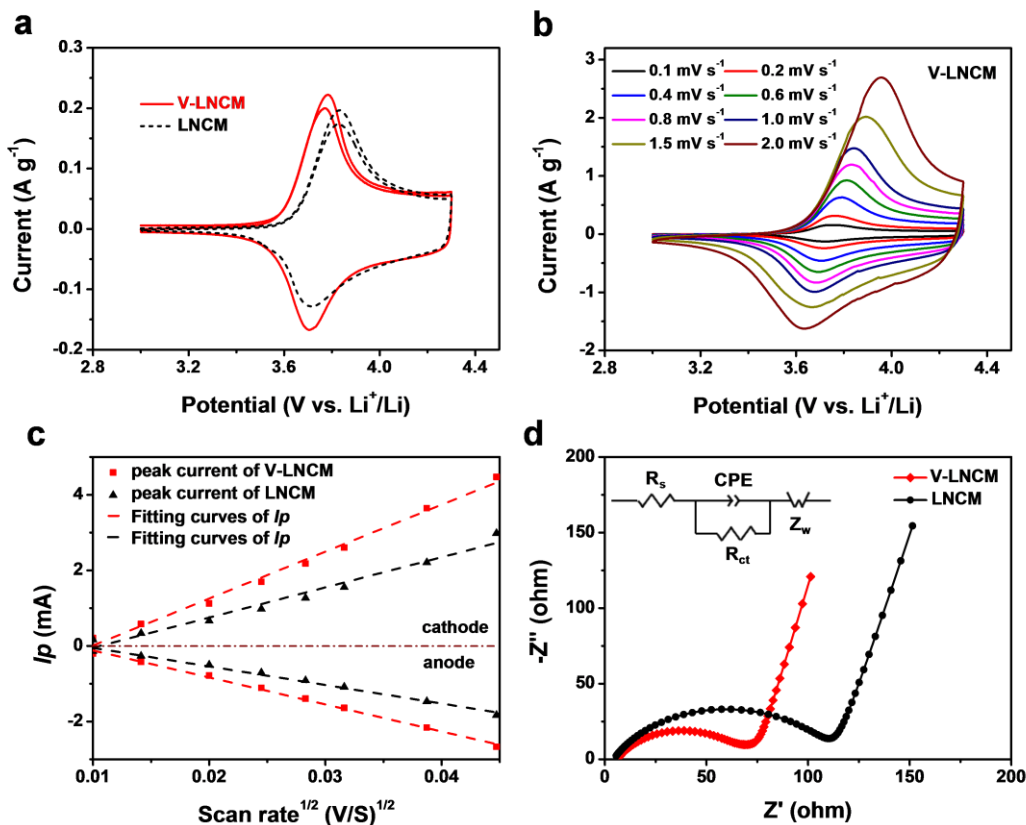
Figure 5. (a) CV curves of LNCM and V-LNCM at 0.1 mV s^{-1}, (b) CV curves of V-LNCM at 0.1–2.0 mV s^{-1}, (c) Linear fitting of I_p *vs.* scan rate$^{1/2}$ curves for the cathodic/anodic peaks, (d) Nyquist plots of LNCM and V-LNCM.

profiles of V-LNCM at different current rates (Figure S4a for LNCM). With the rate increasing, the charge plateaus move to higher potential due to the more serious electrode polarization. Figure S4b displays the comparison of magnified charge profiles. The lower potential in the initial charge curves indicates the better diffusion of ions for V-LNCM.

As shown in Figure 4d and Figure S4c, the V-LNCM exhibits smaller capacity decay than LNCM. The discharge capacities of LNCM and V-LNCM are displayed in Table S2. Even at a high rate of 20 C, an initial discharge capacity of 138 mAh g^{-1} is obtained for V-LNCM, higher than that of the LNCM (122 mAh g^{-1}). After 300 cycles, the discharge capacity of V-LNCM remains 94 mAh g^{-1}, while that of LNCM is only 8 mAh g^{-1}. The rate performances of both samples are further investigated. Under rapid changes of the current rate, the V-LNCM shows stable capacities at each state (Figure 4e). When the rate is decreased back to 0.5 C, 98.6% of the initial capacity is recovered for V-LNCM, better than that of LNCM (95.8%). The results indicate that the introduction of vanadium improves the cyclic reversibility of LiNi$_{1/3}$Co$_{1/3}$Mn$_{1/3}$O$_2$. Compared to previous reports on LNCM, the V-LNCM shows higher specific capacity and better cycling stability [8, 33, 34]. The power density and energy density of LNCM and V-LNCM are shown in Figure S4d. At the same power density, V-LNCM delivers higher energy density than LNCM. When discharging at 20 C, V-LNCM has an energy density of 515.9 Wh kg^{-1}, while that of LNCM is 478.5 Wh kg^{-1}. The higher energy density combining with the higher power density demonstrates the advantages of V-LNCM over pristine LNCM.

To reveal the reason for the enhanced electrochemical performances of V-LNCM, CV and EIS tests are carried out. The initial CV curves are shown in Figure 5a. The redox peaks for the Ni^{2+}/Ni^{4+} redox couple are located at 3.705/3.784 V and 3.715/3.830 V for V-LNCM and LNCM, respectively (there is no Co^{3+}/Co^{4+} redox in CV curves due to the cut-off voltage of 4.3 V) [26]. The potential difference

between the anodic and cathodic peaks of V-LNCM is less than 0.1 V, which indicates a weak polarization for V-LNCM during the electrochemical reaction process involving lithium diffusion in a solid phase and electron transfer across the electrode [35]. Figure 5b and Figure S5 show the CV curves at various scan rates of V-LNCM and LNCM, respectively. Each curve exhibits a typical pair of redox peaks for LiNi$_{1/3}$Co$_{1/3}$Mn$_{1/3}$O$_2$ system between 3.6 and 4.0 V [36-37].

The capacity decay of LiNi$_{1/3}$Co$_{1/3}$Mn$_{1/3}$O$_2$ at high rate is on account of the polarization during charge and discharge processes. The diffusion of Li$^+$ ions in the materials is the key factor to control electrochemical reaction procedure. The Randles-Sevcik equation [38] (Equation (1)) is utilized to calculate the lithium ion diffusion coefficient of V-LNCM and LNCM.

$$I_p = 2.59 \times 10^5 n^{3/2} A D^{1/2} C_0 v^{1/2} \tag{1}$$

where I_p is the peak current (A), n is the number of electrons transferred per molecule (it is 1 for Li$^+$), A is the active surface area of the electrode (cm^2), C_0 is the concentration of lithium ions in the cathode (mol cm^{-3}), D is the apparent ion diffusion coefficient (cm^2 s^{-1}), and v is the scanning rate (V s^{-1}). From the slopes of the fitting lines collected from cathodic/anodic peaks (Figure 5c), the apparent diffusion coefficient D of V-LNCM are calculated to be 9.701×10^{-8} and 3.214×10^{-8} cm^2 s^{-1} for de-lithiation and lithiation processes, higher than those of LNCM (3.285× 10^{-8} and 1.160×10^{-8} cm^2 s^{-1}). The results indicate that the lithium ion diffusion coefficient is enhanced by vanadium doping. The Nyquist plots are shown in Figure 5d. The fitting results show that the charge transfer resistance (R$_{ct}$) of V-LNCM (58 Ω) is much smaller than that of LNCM (109 Ω). This indicates that vanadium-doping indeed improves the charge transfer kinetics. V-LNCM provides more efficient electrons/ions transport than that of LNCM.

According to crystal chemistry and energy band theory, the substitution by high valence element could lead to the appearance of defects and n type semiconductor in the crystal lattice, resulting in the increase of lithium ions diffusion rate through the bulk and the enhanced inherent electronic conduction. In this case, we attribute the increase of lithium ion diffusion to two factors: (1) vanadium-doping suppresses the structural collapse in the de-lithiation process. The bonding energy of V-O is much stronger than that of Ni, Co, and Mn mental-oxyen [14], which means vanadium doping could make the crystal structure more stable. (2) vanadium-doping reduces the Li^+/Ni^{2+} disorder, contributing to rapid diffusion of Li^+ ions. During charge-discharge processes, the decreased Li^+/Ni^{2+} disorder guarantees less obstacle in the diffusion route of Li^+ ions. In addition, the electronic conductivity of V-LNCM can also be enhanced via vanadium-doping, due to the mixed Mn^{3+} and Mn^{4+} with higher electron conduction than pure Mn^{4+} [39]. The enhanced diffusion coefficient of lithium ions and better electronic conductivity can mitigate the polarization in electrode reaction processes and ensure the good high-rate capability for V-LNCM.

4. CONCLUSIONS

Herein, we synthesize vanadium-doped $LiNi_{1/3}Co_{1/3}Mn_{1/3}O_2$ cathode with decreased Li^+/Ni^{2+} disorder, which manifests outstanding long-cycling and high-rate performance. After 1000 cycles at 1 C, the discharge capacity remains 114 mAh g^{-1}, corresponding to 70.9% of its initial capacity. When discharged at 20 C, the specific capacity remains 138 mAh g^{-1}. The splendid property derives from the increase of lithium ions diffusion coefficient and electronic conductivity by the substitution of vanadium. The existence of vanadium improves the concentration of Mn^{3+} ions and reduces the Li^+/Ni^{2+} disorder in the lattice, which are beneficial for the diffusion of Li^+ ions and electrons. The rapid diffusion of Li^+ ions and electrons lead to smaller polarization during electrode reaction processes and contribute to better high-rate capability. Meanwhile, the high bonding energy between vanadium and oxygen guarantees the structural stability when Li^+ ions extract from the lattice, promoting the improvement in long-cycling performance. Our results demonstrate that the vanadium-doped $LiNi_{1/3}Co_{1/3}Mn_{1/3}O_2$ is one of the most attractive cathodes for the practical applications, particularly for the high rate lithium ion batteries in the electric vehicles.

REFERENCES

1. W. Xiong, Y. Jiang, Z. Yang, D. G. Li, Y. H. Huang, J. Alloys Compd. 589 (2014) 615.
2. B. Huang, X. H. Li, Z. X. Wang, H. J. Guo, L. Shen, J. X. Wang, J. Power Sources 252 (2014) 200.
3. Y. X. Hu, T. R. Zhang, F. Y. Cheng, Q. Zhao, X. P. Han, J. Chen, Angew. Chem. Int. Ed. 54 (2015) 4338.
4. J. Guo, L. F. Jiao, H. T. Yuan, H. X. Li, M. Zhang, Y. M. Wang, Electrochim. Acta 51 (2006) 3731.
5. F. Wu, J. Tian, Y. Su, J. Wang, C. Zhang, L. Bao, T. He, J. Li, S. Chen, ACS Appl. Mater. Interfaces 7 (2015) 7702.
6. N. N. Sinha, N. Munichandraiah, ACS Appl. Mater. Interfaces 1 (2009) 1241.
7. K. Araki, N. Taguchi, H. Sakaebe, K. Tatsumi, Z. Ogumi, J. Power Sources 269 (2014) 236.
8. F. Wang, S. Xiao, Z. Chang, Y. Yang, Y. Wu, Chem. Commun. 49 (2013) 9209.
9. W. Luo, F. Zhou, X. Zhao, Z. Lu, X. Li, J. R. Dahn, Chem. Mater. 22 (2010) 1164.
10. T. E. Conry, A. Mehta, J. Cabana, M. M. Doeff, Chem. Mater. 24 (2012) 3307.
11. W. Luo, J. R. Dahn, J. Electrochem. Soc. 158 (2011) A428.
12. D. Liu, Z. Wang, L. Chen, Electrochim. Acta 51 (2006) 4199.
13. N. K. Karan, M. Balasubramanian, D. P. Abraham, M. M. Furczon, D. K. Pradhan, J. J. Saavedra-Arias, R. Thomas, R. S. Katiyar, J. Power Sources 187 (2009) 586.
14. H. Zhu, T. Xie, Z. Chen, L. Li, M. Xu, W. Wang, Y. Lai, J. Li, Electrochim. Acta 135 (2014) 77.
15. H. S. Shin, D. Shin, Y. K. Sun, Electrochim. Acta 52 (2006) 1477.
16. P. Yue, Z. Wang, X. Li, X. Xiong, J. Wang, X. Wu, H. Guo, Electrochim. Acta 95 (2013) 112.
17. X. Liu, P. He, H. Li, M. Ishida, H. Zhou, J. Alloy. Compd 552 (2013) 76.
18. X. Xiong, Z. Wang, G. Yan, H. Guo, X. Li, J. Power Sources 245 (2014) 183.
19. C. S. Sun, Z. Zhou, Z. G. Xu, D. G. Wang, J. P. Wei, X. K. Bian, J. Yan, J. Power Sources 193 (2009) 841.
20. E. Dai, H. Fang, B. Yang, W. Ma, Y. Dai, Ceram. Int. 41 (2015) 8171.
21. L. L. Zhang, H. B. Sun, X. L. Yang, Y. W. Wen, Y. H. Huang, M. Li, G. Peng, H. C. Tao, S. B. Ni, G. Liang, Electrochim. Acta 152 (2015) 496.
22. L. Liao, X. Wang, X. Luo, X. Wang, S. Gamboa, P. J. Sebastian, J. Power Sources 160 (2006) 657.
23. T. Ohzuku, Y. Makimura, Chem. Lett. 30 (2001) 642.
24. X. Zhang, W. J. Jiang, A. Mauger, Qilu, F. Gendron, C. M. Julien, J. Power Sources 195 (2010) 1292.
25. S. T. Myung, K. Izumi, S. Komaba, H. Yashiro, H. J. Bang, Y. K. Sun, N. Kumagai, J. Phys. Chem. C 111 (2007) 4061.
26. W. Hua, J. Zhang, Z. Zheng, W. Liu, X. Peng, X. D. Guo, B. Zhong, Y. J. Wang, X. Wang, Dalton Trans. 43 (2014) 14824.
27. K. M. Shaju, S. Rao, B. V. R. Chowdari, Electrochim. Acta 48 (2002) 145.
28. N. Mansour, Surf. Sci. Spectra 3 (1994) 221.
29. M. Oku, Y. Sato, Appl. Surf. Sci. 55 (1992) 37.
30. W. Wei, W. Chen, D. G. Ivey, Chem. Mater. 20 (2008) 1941.
31. M. Sathiya, A. S. Prakash, K. Ramesha, J. M. Tarascon, A. K. Shukla, J. Am. Chem. Soc. 133 (2011) 16291.
32. K. M. Shaju, P. G. Bruce, Adv. Mater. 18 (2006) 2330.
33. J. Li, S. Xiong, Y. Liu, Z. Ju, Y. Qian, Nano Energy 2 (2013) 1249.
34. F. Fu, G. L. Xu, Q. Wang, Y. P. Deng, X. Li, J. T. Li, L. Huang, S. G. Sun, J. Mater. Chem. A 1 (2013) 3860.
35. P. Gao, Y. Li, H. Liu, J. O. Pinto, X. Jiang, G. Yang, J. Electrochem. Soc. 159 (2012) A506.
36. J. Li, C. Cao, X. Xu, Y. Zhu, R. Yao, J. Mater. Chem. A 1 (2013) 11848.
37. Z. D. Huang, X. M. Liu, S. W. Oh, B. Zhang, P. C. Ma, J. K. Kim, J. Mater. Chem. 21 (2011) 10777.
38. L. Cui, J. Shen, F. Cheng, Z. Tao, J. Chen, J. Power Sources 196 (2011) 2195.
39. M. Kunduraci, J. F. Al-Sharab, G. G. Amatucci, Chem. Mater. 18 (2006) 3585.

Cite this article as:

Zhengyao Hu *et al.*: Vanadium-doped LiNi1/3Co1/3Mn1/3O2 with decreased lithium/nickel disorder as high-rate and long-life lithium ion battery cathode. Sci. Adv. Today 1 (2015) 25218.

LOGNOR
www.lognor.com/scienceadvancestoday